Evaluation of three approaches for simulating 3D time-domain electromagnetic data

Raphael Rochlitz[1], Marc Seidel[2,3], Ralph-Uwe Börner[4]

[1] *Leibniz Institute for Applied Geophysics, Hanover, Germany*

[2] *Institute of Geophysics and Meteorology, University of Cologne, Cologne, Germany*

[3] *GEOMAR Helmholtz Centre for Ocean Research, Kiel, Germany*

[4] *TU Bergakademie Freiberg, Institute of Geophysics and Geoinformatics, Freiberg, Germany*

29 July 2021

SUMMARY

We implemented and compared the implicit Euler time-stepping approach, the inverse Fourier Transform-based approach, and the Rational Arnoldi method for simulating 3D transient electromagnetic data. We utilize the finite-element method with unstructured tetrahedral meshes for the spatial discretization supporting irregular survey geometries and anisotropic material parameters. Both, switch-on and switch-off current waveforms, can be used in combination with direct current solutions of Poisson problems as initial conditions. Moreover, we address important topics such as the incorporation of source currents and opportunities to simulate impulse as well as step response magnetic field data with all approaches for supporting a great variety of applications. Three examples ranging from simple to complex real-world geometries and validations against external codes provide insight into the numerical accuracy, computational performance, and unique characteristics of the three applied methods. We further present an application of logarithmic Fourier transforms to convert transient data into the frequency domain. We made all approaches available in the open-source Python toolbox *custEM*, which previously supported only frequency-domain electromagnetic data. The object-oriented software implementation is suited for further elaboration on distinct modeling topics and the presented examples can serve for benchmarking other codes.

Key words: numerical solutions – electromagnetic theory – finite element method – transient electromagnetics – open-source

1 INTRODUCTION

The transient electromagnetic (TEM) method is widely used for the exploration of marine hydrocarbon reservoirs (Constable 2010; Key 2012b), mineral deposits (Smith 2014; Guo et al. 2020) and groundwater (Siemon et al. 2009; Yogeshwar & Tezkan 2017). Nowadays, applications comprise different scales in airborne, land-based, marine and mixed setups. Fast and robust forward modeling techniques are not only required for the inversion of the recorded data for the increasingly complex, large-scale 3D setups (Börner 2010), but also for investigating the effects of geological structures and optimizing survey designs.

Electromagnetic (EM) responses in the fields of magnetotellurics (MT), controlled-source EM (CSEM) and TEM were simulated for decades using field or potential formulations based on Maxwell's equations in either frequency domain ($\mathcal{FD}$) or time domain ($\mathcal{TD}$). Solutions to these formulations are reported by, e.g., Anderson (1973); Schmucker & Weidelt (1975); Kaufman et al. (1983) for 1D layered-earth geometries with single anomaly bodies, and by, e.g., Oristaglio (1982); Goldman & Stoyer (1983) for 2D cases. Raiche (1974); Hohmann (1975); Druskin & Knizhnerman (1988); Wang & Hohmann (1993); Alumbaugh et al. (1996); Commer & Newman (2004) present first applications in 3D using the integral equation and finite-difference (FD) methods. Early 3D applications of the finite-element (FE) and finite-volume methods are reported by, e.g., Coggon (1971); Pridmore et al. (1981); Madsen & Ziolkowski (1990); Haber et al. (2000).

During the last two decades, the FE method gained attraction due to the suitability for discretizing realistic subsurface geometries using unstructured meshes as well as the increasing availability of computational resources (e.g., Badea et al. 2001; Um et al. 2010; Schwarzbach et al. 2011; Farquharson & Miensopust 2011; Ren et al. 2013; Grayver & Kolev 2015; Börner et al. 2015). More and more MT, CSEM and TEM modeling codes support topography or bathymetry, anisotropic electric conductivities, or induced polarization effects. The most recent developments comprise not only the FE method (e.g., Liu et al. 2018a; Lin et al. 2018; Qiu et al. 2019b; Qi et al. 2019; Kamm et al. 2020), but also finite-difference, integral equation, finite-volume, hybrid, meshless, and other methods (e.g., Cherevatova et al. 2018; Kruglyakov & Kuvshinov 2019; Long & Farquharson 2019; Bello et al. 2019; Huang et al. 2019; Lu et al. 2019).

Even though there are numerous publications in the field of geophysical 3D EM modeling, there is still a great demand for open-source 3D codes which support complex setups and serve to validate individual numerical implementations (Miensopust 2017). In this context, the term open-source is referred to as software tools which are independently accessible and usable by scientists without requesting authors' permission explicitly. The multi-geophysics modeling and inversion tools provided by *SimPEG* (Cockett et al. 2015) and *pyGIMLi* (Rücker et al. 2017) were already made available to the community several years ago. Recently, Castillo-Reyes et al. (2018); Rochlitz et al. (2018); Werthmüller et al. (2019b) present the open-source codes *PETGEM* (FE), *custEM* (FE) and *emg3d* (FD) as tools for simulations in the frequency domain. For 3D time-domain EM modelings, there are tools in the *P223F* software suite (Raiche et al. 2007) or in *SimPEG* (Heagy et al. 2020) openly available. Most recently, Werthmüller et al. (2021) presents time-domain modeling techniques using *emg3d*, which were in simultaneous development to our work.

We present the first direct comparison of three established techniques for simulating TEM data. In particular, we considered the implicit Euler time-stepping method, an approach based on Fourier-transformed frequency-domain solutions, as well as a Rational Arnoldi method. We analyze the three time-domain approaches, focus on supporting complex 3D geometries with unstructured tetrahedral meshes and compare results obtained with all three approaches in terms or accuracy and computational performance.

The following section introduces the underlying methodology of the three time-domain modeling approaches. Afterwards, we describe details about the implementation. The numerical examples provide insights about the accuracy and required computational resources of our implemented approaches. The first example deals with a land-based TEM setup and a loop transmitter (Tx) over a simple 1D structure, enabling a comparison between our solutions and semi-analytic references obtained with *empymod* (Werthmüller 2017). The second example uses a long-offset TEM (LOTEM) setup on a larger scale with a grounded wire source over a blocky 3D structure. Our results are compared with solutions of the *SLDMEM* software, which is based on the work by Druskin & Knizhnerman (1994). The third shows the capability of *custEM* to handle configurations which might be relevant to potential needs of the exploration industry. We computed EM responses of the Marlim R3D model (Correa & Menezes 2019) using the Rational Arnoldi method and compared the Fourier-transformed results to the reference solutions in the frequency domain. Before drawing our conclusions, we discuss the pros and cons of all approaches as well as potential optimization possibilities and general limitations.

2 METHODOLOGY

In this section, we provide the fundamentals of the three considered numerical approaches for simulating time-domain electromagnetic data. At first, we define the underlying partial differential equations for the given EM problem. We introduce a numerically feasible spatial discretization of the Maxwell equations with finite-element methods afterwards. For this purpose, we closely follow Ward & Hohmann (1988) and Jin (2015).

We consider a bounded domain $\Omega \subset \mathbb{R}^3$ with the outer unit normal $\mathbf{n}$ and the spatially dependent, general electric conductivity tensor $\sigma = \sigma_{ij}(\mathbf{r})$, defined on Ω. Neglecting displacement currents, the derived time-dependent partial differential equation for the electric field $\mathbf{e} = \mathbf{e}(\mathbf{r}, t)$ reads

$$\nabla \times \mu^{-1} \nabla \times \mathbf{e} + \sigma \frac{\partial \mathbf{e}}{\partial t} = -\frac{\partial \mathbf{j_e}^t}{\partial t}, \quad t \in \mathbb{R}, \tag{1}$$

where $\mu = \mu(\mathbf{r})$ denotes the magnetic permeability, and $\mathbf{j}_e^t$ the source current density function

$$\mathbf{j_e}^t = \mathbf{j_e}^t(\mathbf{r}, t) = \mathbf{q}(\mathbf{r})s(t), \tag{2}$$

with $\mathbf{q}$ being the spatial pattern of the source current and s the temporal current waveform. The latter simplifies to a Heaviside step function $H(t)$ or $H(-t)$ for a transmitter switch-on or switch-off, respectively, at time $t = 0$ which is convenient for approximating the current waveforms of many TEM systems.

Along the boundary $\partial\Omega$ of Ω, we impose the inhomogeneous Dirichlet boundary condition

$$\mathbf{n} \times \mathbf{e} = \mathbf{n} \times \mathbf{g}, \tag{3}$$

where the boundary data $\mathbf{g} : \partial\Omega \to \mathbb{R}^3$ can be modeled as the solution of simplified models such as a layered half-space. With the implicit assumption that the boundaries are sufficiently far away from the source, Equation 3 reduces to the homogeneous Dirichlet condition

$$\mathbf{n} \times \mathbf{e} = \mathbf{0}. \tag{4}$$

In addition, Neumann boundary conditions can be defined as

$$\mathbf{n} \times \mu^{-1} \nabla \times \mathbf{e} = \mathbf{0}. \tag{5}$$

The combination of Equation 1 and Equation 3 results in the initial-value problem

$$\nabla \times \mu^{-1} \nabla \times \mathbf{e} + \sigma \frac{\partial \mathbf{e}}{\partial t} = -\frac{\partial \mathbf{j_e}^t}{\partial t} \qquad \text{on } \Omega \times (0, \infty), \tag{6a}$$

$$\sigma \mathbf{e}|_{t=0} = \mathbf{q} \qquad \text{on } \Omega, \tag{6b}$$

$$\mathbf{n} \times \mathbf{e} = \mathbf{n} \times \mathbf{g} \qquad \text{on } \partial\Omega \times (0, \infty). \tag{6c}$$

The same problem can be formulated in the frequency domain. We apply the Fourier transform, denoted by $\mathcal{F}$, and introduce the electric field $\mathbf{E}$ in the frequency domain as a function of the angular frequency ω

$$\mathbf{e}(\mathbf{r}, t) := \mathcal{F}(\mathbf{E}(\mathbf{r}, \omega)) = \frac{1}{2\pi} \int\limits_{-\infty}^{\infty} \mathbf{E}(\mathbf{r}, \omega) e^{i\omega t} \, d\omega. \qquad \omega \in \mathbb{R}. \tag{7}$$

We obtain the frequency-domain problem with the scaling and derivative laws of the Fourier transform

$$\nabla \times \mu^{-1}\nabla \times \mathbf{E} + i\omega\sigma\mathbf{E} = -i\omega\mathbf{j_e} \qquad\qquad \text{on } \Omega \times (0, \infty) \tag{8}$$

$$\mathbf{n} \times \mathbf{E} = \mathbf{n} \times \mathbf{G}, \qquad\qquad \text{on } \partial\Omega \tag{9}$$

with complex-valued electric fields $\mathbf{E} : \Omega \to \mathbb{C}^3$ and boundary data $\mathbf{G} : \partial\Omega \to \mathbb{C}^3$.

The spatial approximation of both formulations is based on a finite-element discretization using first (p1) and second (p2) order Nédélec elements (Nédélec 1980) on unstructured tetrahedral meshes.

We employ a standard variational formulation for Maxwell's equations and define the restricted Sobolev space

$$\boldsymbol{H}_0(\mathrm{curl}; \Omega) = \left\{ \boldsymbol{u} \in L^2(\Omega) : \nabla \times \boldsymbol{u} \in L^2(\Omega), \quad \mathbf{n} \times \boldsymbol{u} = \mathbf{0} \text{ along } \partial\Omega \right\}, \tag{10}$$

where $L^2(\Omega)$ denotes the function space of square-integrable vector fields on Ω. The weak formulation in $\mathcal{TD}$ is obtained by multiplying Equation 1 by a stationary and smooth vector-valued test function $\phi \in \boldsymbol{H}_0(\mathrm{curl}; \Omega)$ and applying integration by parts.

This yields the weak form of the variational problem in the time domain

$$\left(\mu^{-1}\nabla \times \mathbf{e}, \nabla \times \boldsymbol{\phi}\right) + (\sigma\partial_t\mathbf{e}, \boldsymbol{\phi}) = \mathbf{0}, \quad t \in (0, \infty) \tag{11}$$

$$(\sigma\mathbf{e}|_{t=0}, \boldsymbol{\phi}) = (\mathbf{q}, \boldsymbol{\phi}), \tag{12}$$

for all $\boldsymbol{\phi} \in \boldsymbol{H}_0(\mathrm{curl}; \Omega)$, where $(\cdot, \cdot)$ denotes the inner product on $L^2(\Omega)$, i.e.,

$$(\mathbf{u}, \mathbf{v}) = \int_\Omega \mathbf{u} \cdot \overline{\mathbf{v}}\, d\Omega, \tag{13}$$

with $\overline{\mathbf{v}}$ as the complex conjugate of $\mathbf{v}$. The weak form can be made numerically computable by further restricting the Sobolev space to a finite-dimensional subspace consisting of Nédélec finite elements on a tetrahedral mesh $\mathcal{T}_h$. On each tetrahedron $K \in \mathcal{T}_h$, the functions in the finite-dimensional subspace of $\boldsymbol{H}_0(\mathrm{curl}; \Omega)$ consist of vector polynomials.

Using the Galerkin method and expanding the discrete solution of the above variational problem in a basis $[\phi_1, \ldots, \phi_N]$, solving Equation 1 becomes the solution of the semi-discrete initial-value problem of the ordinary differential equation

$$\mathbf{C}\mathbf{u}(t) + \mathbf{M}\partial_t\mathbf{u}(t) = \mathbf{0}, \quad t \in (0, \infty), \quad \mathbf{M}\mathbf{u}(0) = \mathbf{s}, \tag{14}$$

where the vector $\mathbf{u}(t)$ contains the N coefficients of the finite element approximation of $\mathbf{e}(t)$ inside the computational domain with respect to the Nédélec basis at time $t > 0$.

The mass matrix $\mathbf{M}$, the curl-curl matrix $\mathbf{C}$, as well as the vector $\mathbf{s}$ are given in terms of the Nédélec basis by

$$[\mathbf{M}]_{ij} = \int_\Omega \boldsymbol{\phi}_i \cdot (\sigma\boldsymbol{\phi}_j)\, d\Omega, \tag{15}$$

$$[\mathbf{C}]_{ij} = \int_\Omega (\nabla \times \boldsymbol{\phi}_i) \cdot (\mu^{-1}\nabla \times \boldsymbol{\phi}_j)\, d\Omega, \tag{16}$$

$$[\mathbf{s}]_i = \int_\Omega \mathbf{q} \cdot \boldsymbol{\phi}_i\, d\Omega \text{ for } i, j = 1, \ldots, N. \tag{17}$$

2.1   Implicit Euler method – IE

Following Um et al. (2010) or Cai et al. (2017) with geophysical applications, we use an implicit Euler (IE) time-integration scheme to solve Equation 1 in time. The advantage over explicit Euler methods is that the solution is unconditionally stable (e.g., Jin 2015). With $\mathbf{u}(t)$ as a numerical approximation to $\mathbf{e}(t)$ and discrete time steps Δt, the first-order backward Euler scheme reads

$$\left(\mathbf{C} + \Delta t\,\mathbf{M}\right)\mathbf{u}^{n+1} = \mathbf{C}\,\mathbf{u}^n + \Delta t\,\mathbf{s}^{n+1}\,. \tag{18}$$

The solution $\mathbf{u}^{n+1}$ at time $t_{n+1} = t_n + \Delta t$ depends only on the solution at time t_n. Using the second-order accurate scheme, which is superior in case of a non-linear behavior of $\mathbf{j_e}^t$ (Um et al. 2010) , the solution $\mathbf{u}^{n+2}$ is based on the results $\mathbf{u}^{n+1}$, $\mathbf{u}^n$ of two previous time steps

$$\left(3\mathbf{C} + 2\Delta t\,\mathbf{M}\right)\mathbf{u}^{n+2} = 4\mathbf{C}\,\mathbf{u}^{n+1} - \mathbf{C}\,\mathbf{u}^n - 2\Delta t\,\mathbf{s}^{n+2}. \tag{19}$$

With $\mathbf{b}$ denoting the magnetic flux density and • the first time derivative, magnetic fields can be derived using the relation

$$\nabla \times \mathbf{e} = \mu\frac{\partial \mathbf{h}}{\partial t} = \dot{\mathbf{b}}\,. \tag{20}$$

Most land-based transient CSEM methods require a time discretization of several decades between 1 μs and 1 s or even later times in marine setups. Related to the decay behavior of electric fields, logarithmically increasing times steps appear to be adequate for covering these time ranges. However, Um et al. (2010) point out that piece-wise constant time steps can significantly increase the performance, because the system matrix factorization can be reused for all these steps. In contrast to different concepts of adaptive time stepping techniques (Um et al. 2010, 2012; Cai et al. 2017), we considered a generally practical approach. We first divided the complete time range into n_{log} logarithmic intervals and afterwards, each of them into n_{lin} uniform linear steps. This resulted in only n_{log} matrix factorization and $n_{log} \cdot n_{lin}$ solution phases with the direct solver *MUMPS*. Electric and magnetic fields were interpolated and exported at each logarithmic step. This is the default setting, but user-defined time stepping sequences and custom points in time for the stored fields are supported.

2.2   Fourier Transform based methods – FT

Fourier Transform (FT) based methods convert frequency-domain data into the time domain. The $\mathcal{FD}$ solutions are, for instance, obtained based on Equation 8 (Rochlitz et al. 2019). The majority of publications dealing with $\mathcal{TD}$ CSEM forward simulations used such Fourier-based approaches based on sine/cosine, Laplace or Hankel transforms. The greatest challenge of these approaches is to minimize the amount of computationally expensive $\mathcal{FD}$ forward modeling to obtain a single $\mathcal{TD}$ solution. The transforms themselves are of negligible computational effort.

Ghosh (1971) introduces the first application of the digital linear filter (DLF) method for Fast Hankel transforms (FHT) of Schlumberger and Wenner DC resistivity sounding data. Johansen & Sørensen (1979); Andersen (1989); Christensen (1990); Mohsen & Hashish (1994) further develop this method. Börner et al. (2008) combine a simple

Rational Arnoldi method to evaluate solutions of 3-D Maxwell's equations in the frequency domain and obtain the time-domain solution by a subsequent FHT. Recently, Werthmüller et al. (2019a) present a comparison of different Hankel- and Fourier Transform methods and confirmed that the FHT with digital filters is very well suited for frequencies in the range of CSEM modeling.

We utilize the FHT for evaluating integrals of the form

$$g(r) = \int_0^\infty f(k) \, J_\nu(kr) \, dk, \quad \nu > -1 \,. \tag{21}$$

In general, these kinds of integrals are called Hankel Transforms, with a function $f(k)$ to be transformed and $J_\nu(kr)$ being the Bessel function of the first kind and order $\nu > -1$. Because of the oscillatory behavior of the Bessel function, the evaluation of such an integral would be numerically quite expensive for large arguments kr. These numerical costs can be significantly reduced by the FHT, which uses digital linear filter coefficients ($\hat{H}$) for a fast computation of the Hankel integral by casting it into a discrete sum

$$g(r) \approx \frac{1}{r} \sum_n f_n \, \hat{H}_{m-n}. \tag{22}$$

Both, computational speed and numerical accuracy requirements, determine the choice of the digital filters when using the FHT. Typical filter sets contain a minimum of 50 to 100, on average 100 to 200 and in some cases up to several hundred coefficients (Key 2012a; Werthmüller et al. 2019a). More coefficients usually provide a higher accuracy, but it is also possible to achieve sufficiently accurate transform results with only a few tens of filter coefficients (Werthmüller et al. 2021) which significantly influences the computation times. In this work, we use a digital linear filter set for the sine transform ($\nu = -\frac{1}{2}$) that consists of $n = 80$ coefficients (Appendix A). They were optimized based on the work by Christensen (1990). Using only 80 filter coefficients allows for a comparatively fast computation of the $\mathcal{TD}$ solution yet providing a sufficient accuracy (Seidel 2019). The coefficients were designed for 10 time channels per decade and are well suited for most land-based CSEM applications.

2.3   Rational Arnoldi method – RA

After discretization in space, the explicit solution of the semi-discrete time-domain problem (14) is given in terms of the matrix-exponential function (Börner et al. 2015)

$$\mathbf{u}(t) = \exp(-t\mathbf{M}^{-1}\mathbf{C})\mathbf{M}^{-1}\mathbf{s} = f(\mathbf{A})\mathbf{u}_0, \quad \mathbf{A} = \mathbf{M}^{-1}\mathbf{C}, \tag{23}$$

with the initial solution

$$\mathbf{u}_0 = \mathbf{M}^{-1}\mathbf{s}. \tag{24}$$

When the matrices $\mathbf{C} \in \mathbb{R}^{N \times N}$ and $\mathbf{M} \in \mathbb{R}^{N \times N}$ are large and sparse, Krylov subspace methods can be used to obtain an efficient approximation of the product of the matrix-exponential in Equation (23) with a vector.

We use a rational Krylov orthogonalization algorithm to construct a sequence of orthonormal vectors $\{\mathbf{v}_j\}_{j \geq 1}$. Starting this sequence with $\mathbf{v}_1 = \mathbf{u}_0/\|\mathbf{u}_0\|$, we determine in each step a vector $\mathbf{v}_{j+1}$ which is orthogonal to the

previously generated vectors $\mathbf{v}_1, \ldots, \mathbf{v}_j$. This leads to the recursion

$$\mathbf{v}_{j+1} h_{j+1,j} = (\mathbf{A} - \xi_j \mathbf{I})^{-1} \mathbf{v}_j - \sum_{i=1}^{j} \mathbf{v}_i h_{i,j}, \quad j = 1, 2, \ldots, m, \tag{25}$$

where $h_{i,j}$ are the elements of an upper Hessenberg matrix computed by the Arnoldi algorithm, and the coefficients $\{\xi_j\}_{j=1,\ldots,m}$ are known as poles.

The numerical effort of recursion in Equation (25) is dominated by the repeated solution of large linear systems of the form

$$\mathbf{v}_{j+1} \leftarrow (\mathbf{A} - \xi_j)^{-1} \mathbf{v}_j. \tag{26}$$

Once the set of basis vectors $\mathbf{V}_{m+1} = [\mathbf{v}_1, \mathbf{v}_2, \ldots, \mathbf{v}_{m+1}]$ has been computed, we can define the rational Arnoldi approximation for $f(\mathbf{A})\mathbf{u}_0$ of order m as

$$\mathbf{f}_m := \|\mathbf{u_0}\| \mathbf{V}_{m+1} f(\mathbf{A}_{m+1}) \mathbf{e}_1, \quad \mathbf{A}_{m+1} := \mathbf{V}_{m+1}^\top \mathbf{A} \mathbf{V}_{m+1}, \tag{27}$$

where $\mathbf{e}_1 = [1, 0, \ldots, 0]^\top$ is the first unit-vector in $\mathbb{R}^{m+1}$. The matrix $\mathbf{A}_{m+1}$ is the projection of $\mathbf{A}$ with respect to $\mathbf{V}_{m+1}$. It is of size $(m+1) \times (m+1)$. Since $m \ll N$, computing $f(\mathbf{A}_{m+1})$, or, more precisely, computing the expression $\exp(-t\mathbf{A}_{m+1})$ becomes feasible, whereas the effort to compute $\exp(-t\mathbf{A})$ is prohibitive.

It remains to determine the coefficients ξ_j in Equation (25). Börner et al. (2015) have proposed a surrogate problem to find optimal values for the coefficients ξ_j. Their suggested method reduced the problem of finding m parameters to that of finding merely ℓ parameters corresponding to only $\ell < m$ distinct shifts in the linear system solves in Equation (25). Reusing the shifts for the Arnold iterations makes the employment of direct solvers suitable.

In this work, we used a new set of $\ell = 2$ cyclically repeated distinct poles $\xi_1 = 323.1722, \xi_2 = 6.0128 \times 10^5$ and $m = 48$ rational Krylov subspace iterations to cover time intervals of four to five decades with one simulation. The logarithmic range $[t_0, t_1]$ (e.g., 10^{-4} to 1 s) can be adjusted by multiplying the poles by $10^{-6-\log_{10}(t_0)}$. Accordingly, the FE simulations require only three matrix factorizations, i.e., one for the computation of $\mathbf{u}_0$ and two associated with the poles ξ_1 and ξ_2.

2.4 Static fields

We consider switch-on as well as switch-off transients of the common 50 % duty-cycle square-wave current function. Switch-on and switch-off transients can be converted into each other in case of knowing the static electric or magnetic field. If the switch-off response of $\mathbf{b}$ is of interest, the static magnetic field $\mathbf{b}_{\text{static}}$ of grounded or ungrounded sources can be calculated analytically with the Biot-Savart law. Obtaining switch-off $\mathbf{e}$-field transients can be achieved by calculating or approximating the direct current (DC) field $\mathbf{e}_{\text{dc}}$.

The DC field can be obtained by solving the Poisson problem with the FE method (e.g., Um et al. 2010)

$$\nabla \cdot (\sigma \nabla \Phi) = -\nabla \cdot \mathbf{j_e} \tag{28}$$

$$\mathbf{e}_{\text{dc}} = -\nabla \Phi \tag{29}$$

where Φ is the electric potential. In addition to the commonly preferred secondary field formulation of this problem (Um et al. 2010), we considered a total-field formulation by incorporating the divergence of the source current directly on the two grounding nodes of the Tx. The total-field formulation supports arbitrary model geometries with topography. If e_{dc} is directly projected onto the tetrahedral edges (in the Nédélec FE space) from Φ evaluated at the nodes (in the Lagrange FE space), we found that both approaches lead to almost identical results. We recommend using second order (p2) basis functions for solving the Poisson-problem with a significantly higher accuracy compared to those obtained with p1 basis functions.

Alternatively, e_{dc} and also b_{static} might be approximated by a low-frequency solution (< 0.001 Hz) of the quasi-static EM problem. The **FT** approach provides such a solution automatically, but we found that this approximation is often not accurate enough for reliably deriving the late-time response of switch-off transients. Instead, calculating static fields can be avoided for obtaining switch-off transients with the **FT** approach by using an additional cosine transform with other filter coefficients. We considered only the sine transform with explicitly calculated static fields in this work.

Our preferred way of simulating a switch-off process with the **IE** approach is to implement two subsequent source pulses with a switch-on phase in between (e.g., 10 s with 10 linear steps of 1 s for land-based TEM). This method necessitates only one additional matrix factorization and a few back-substitutions during the solution phase, which is computationally cheaper than solving the DC problem.

2.5 Magnetic field response

Even though e and $\dot{b}$ are commonly the target quantities in TEM surveys, specific applications may require the simulation of the magnetic field. For instance, modern highly sensitive receivers based on superconducting quantum interference devices (SQUID), optically pumped magnetometers (OPM), or specific coil sensors record b and not the time rate of change of the magnetic field. Such instruments utilized for TEM recordings need appropriate modeling and inverse modeling tools (Rochlitz et al. 2018).

Using the presented **IE** approach, time-integrating Equation 18 and Equation 20 and comparing both equations yield that b is obtained if j_e^t instead of $\dot{j}_e^t$ is defined as the source term on the right-hand side of Equation 18. The step response b is obtained using the step current function j_e^t on the right-hand side, whereas the impulse response $\dot{b}$ and e can be calculated with an impulse-like current function, which itself is the time derivative of a perfect step excitation or Heaviside function.

Dividing the frequency-domain results by $i\omega$ before carrying out the fast Hankel transformation leads to the step response b in the **FT** approach. The only way to obtain b with the **RA** approach is to integrate $\dot{b}$. This method requires a sufficient sampling of $\dot{b}$ over time. We found that 80 frequencies per decade with equidistant spacing along a logarithmic frequency axis led to accurate integrals. The switch-on and switch-off step responses are obtained by integrating $\dot{b}$ in normal or reverse order in time, respectively.

3 IMPLEMENTATION

3.1 custEM

The *custEM* toolbox was initially designed for the robust and automated modeling of complex 3D semi-airborne $\mathcal{FD}$ CSEM data in an object-oriented environment as described by Rochlitz et al. (2019); Rochlitz (2020). We focus on the time-domain modeling specific content and refer to Appendix B for additional details about the software and its development over the past years. The following links forward to the documentation and the source code:

- `https://custem.readthedocs.io`, (19.07.2021)
- `https://gitlab.com/Rochlitz.R/custEM`, (19.07.2021)

3.2 Source current incorporation

We adapted the procedure for incorporating time-independent source currents along edges associated with the transmitter wire, exploiting the characteristics of Nédélec basis functions (Rochlitz et al. 2019). The **FT** method can directly re-use this procedure, which was developed for simulations in $\mathcal{FD}$. Our formulation of the **RA** method is based on perfect initial conditions without ramp effects. Therefore, the source current is treated as constant and can be incorporated in the same way as in $\mathcal{FD}$.

In contrast, the **IE** method requires a modification to account for currents varying over time and also a suitable numerical approximation of the perfect switch-on or switch-off case. Either the source current function $\mathbf{j_e}^t$ or it's time derivative $\overset{\bullet}{\mathbf{j_e}}^t$ needs to be specified on discrete points in time during the on-time. **Figure 1** illustrates two typical source currents in terms of $\overset{\bullet}{\mathbf{j_e}}^t$ as well as $\mathbf{j_e}^t$, a perfect switch-off current in a) and a linear switch-off-ramp in b). Related to the complexity of the time-dependent source functions, a few uniform time steps are appropriate for describing perfect rectangular functions or linear ramps, whereas more steps are required for accurately describing complex source functions. Uniform steps are preferred as they require only one matrix factorization and further inexpensive back-substitutions.

Following Cai et al. (2017) for the commonly considered perfect switch-off case, we consider a Gaussian function (**Figure 1a**) to express the source function of a perfect switch-on or switch-off process at time t_0 in terms of $\overset{\bullet}{\mathbf{j_e}}^t$. We use the following representation of a time-dependent Dirac distribution

$$\overset{\bullet}{\mathbf{j_e}}^t(t) = \hat{\mathbf{j}} \frac{1}{\alpha \sqrt{\pi}} \, \mathrm{e}^{-(t/\alpha)^2}, \qquad \alpha \to 0, \tag{30}$$

where $\hat{\mathbf{j}}$ denotes the current strength of the related step-response signal. We found that suitable choices for α, controlling the stretching of the distribution, are one to three orders of magnitude lower than the earliest observation time (e.g., $\alpha = 10$ ns for $t_0 = 0$ s and the first observation at 1 µs). The smaller α becomes, the better is the approximation of a perfect switch-off current often used for theoretical analysis. Using 100 uniform time steps for the discretization of the source pulse in the range $[t_0 - 5 \cdot \alpha, t_0 + 5 \cdot \alpha]$ showed to result in good accuracy and computational performance.
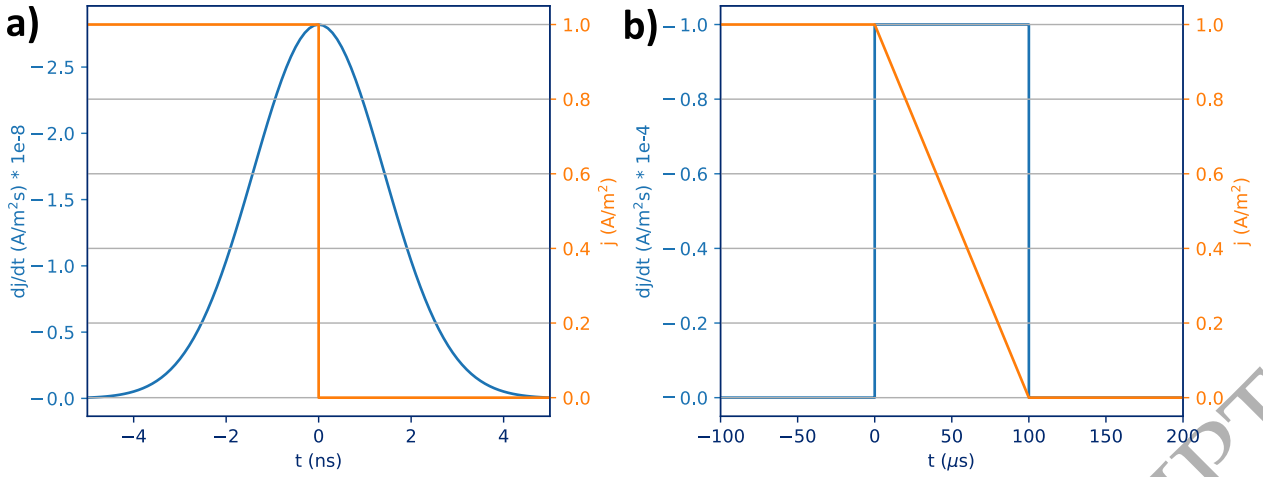
Figure 1. Transmitter current functions in terms of impulse ($\dot{\mathbf{j}}_{\mathbf{e}}^t$) and step ($\mathbf{j}_{\mathbf{e}}^t$) waveforms, a) perfect switch-off of $\mathbf{j}_{\mathbf{e}}^t$ with numerically suitable Gaussian pulse representation of the corresponding $\dot{\mathbf{j}}_{\mathbf{e}}^t$ waveform ($\alpha = 2\,\text{ns}$, interval length is $10\,\text{ns}$), b) $\mathbf{j}_{\mathbf{e}}^t$ and corresponding $\dot{\mathbf{j}}_{\mathbf{e}}^t$ waveforms for a linear switch-off ramp.

4   RESULTS

This section demonstrates the numerical accuracy and computational performance of the implemented algorithms by three examples. All computations were run on a Dell® PowerEdge R940 server with four Intel® Xeon® Gold 6154 processors and 48 LRDIMM 64 GB, DDR4-2666 Quad Ranks shared random access memory (RAM). Over-all, 144 computing nodes and approximately 3 TB RAM were available. We realized parallelization utilizing both *MPI* (*mpi4py*) and *OpenMP*. *MPI* is the default parallel-communication library in *FEniCS* for organizing the mesh distribution with *PETSc* and the parallelized inter-node communication with *MUMPS*. *OpenMP* is a shared-memory library used by *MUMPS* internally for solving the systems of equations, distributing the tasks during this phase over multiple threads. The consumed RAM (Table 1) depends only on the number of parallel *MPI* processes and is not increased by enabling additional *OpenMP* threads. A combined usage of up to tens of *MPI* processes with a few *OpenMP* threads can often reduce the computation times (CT) and memory requirements in FE problems with com-paratively large system sizes, especially for p2 computations (Rochlitz 2020). We used a slightly increased number of *MPI* processes for the **FT** approach to account for the larger systems in the frequency-domain.

4.1   Example #1: Loop transmitter on top of a three-layered earth

First, we investigate the performance of the three implemented approaches using a simple land-based TEM setup with a loop transmitter as illustrated in **Figure 2**. Layered-earth-like geometries usually require a tremendous amount of el-ements for a sufficiently large computational domain to avoid boundary effects. As a compromise, we used a bounded, $4 \times 4\,\text{km}^2$ large fraction of the layered earth embedded within a ten times larger homogeneous halfspace, which led to approximately 17,000 nodes. We set the resistivity of the uppermost layer also for the surrounding boundary-halfspace
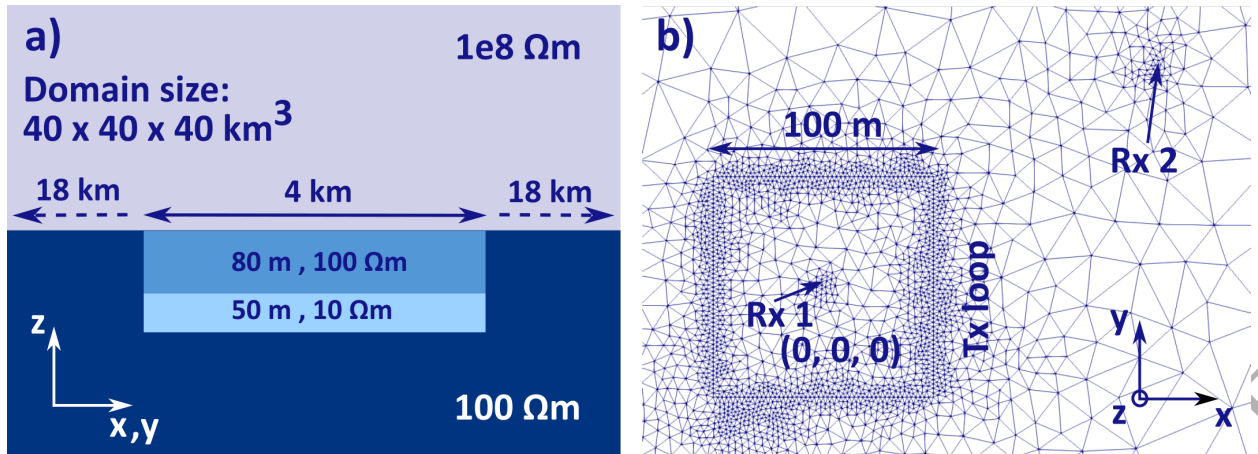
Figure 2. Mesh design for Example #1, a) sketch of layered-earth geometry with a halfspace-like boundary mesh, b) mesh surface view of the Tx-Rx setup.

instead of an averaged value of the three layer resistivities, because a homogeneous lateral continuation of the uppermost layer with the strongest resistivity contrast to the air domain usually leads to the smallest artifacts (Rochlitz 2020).

Table 1 lists the corresponding computational statistics for all considered approaches. We validated our results against the semi-analytic solutions by *empymod* (Werthmüller 2017). **Figure 3** shows the absolute values of $\partial b_z / \partial t$ and b_z at the central loop position. All approaches exhibited overall errors of maximum 10 % for the p1 and 1 % for the p2 computations. The b_z switch-off responses showed increasing errors, dependent on the particular numerical approach, during the latest observation times. The calculations of $\mathbf{b}$ with the integrated formulation of the **IE** approach ($\mathbf{j_e}$ as source instead of $\dot{\mathbf{j}}_{\mathbf{e}}^t$) appeared to be more affected by the domain-size than the standard formulation. An even stronger effect of the domain boundary was visible in the switch-off **FT** results of $\mathbf{b}$. The increasing late-time errors of the switch-off response could be explained by the insufficient estimation of $\mathbf{b}_{\text{static}}$ by the lowest-frequency **B**-field solution, which was influenced by boundary effects as well. If $\mathbf{b}$ is obtained via simple numerical integration as in the **RA** approach, no systematic late-time errors could be observed. Appendix C contains the corresponding switch-on responses and further explanations for interested readers.

Aside from the late time, the **FT** and **RA** results were almost identical, whereas the **IE** errors slightly differed below the level of 1 %. This behavior was attributed to effects of the time-discretization in addition to the influence of the spatial discretization, which dominated the error distribution of all three approaches.

Figure 4 shows the horizontal switch-off e_y and $\partial b_y / \partial t$ responses at the out-of-loop Rx positions. Analogous to the presented central loop results, the average error levels amounted to 10/1 % for p1/p2 and the time-discretization had an unique effect on the **IE** results. The sign reversal in the $\partial b_y / \partial t$ result at 0.02 ms corresponded to the highest relative errors observed.
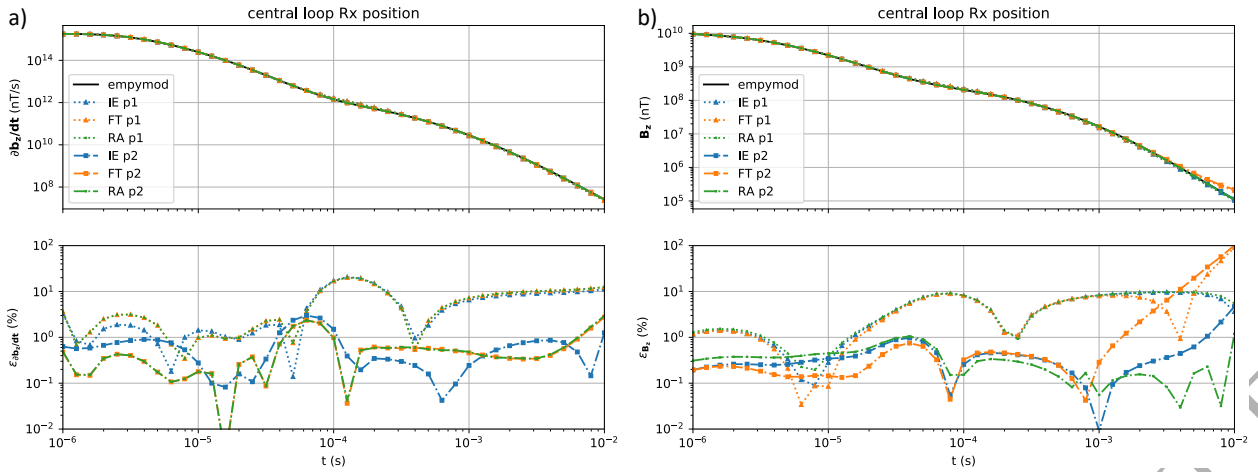
Figure 3. Vertical component of a) magnetic field impulse and b) switch-off step responses at the central loop Rx position, computed with all three approaches and p1 or p2, respectively.

4.2 Example #2: 3D LOTEM with conductors

After presenting a validation against analytic solutions, we considered a 3D LOTEM configuration with a 1 km long dipole source in a halfspace model with three conductive bricks. **Figure 5** illustrates the geometry. **Table 2** provides details about the incorporated anomalies. Solutions obtained with the established *SLDMEM* code, which is based on the work by Druskin & Knizhnerman (1994), served as a reference. To calculate the misfit between the two inexact numerical solutions, we utilized the so-called symmetric mean absolute percentage error (SMAPE) $200 \cdot |a-b|/(|a|+|b|)$.

The parallel simulations were run on a single mesh, whereas the serial *SLDMEM* calculations used six optimized grids for the three receiver lines with respect to $\mathbf{e}$ or $||\partial \mathbf{b}/\partial t||$, respectively. The corresponding computational statistics
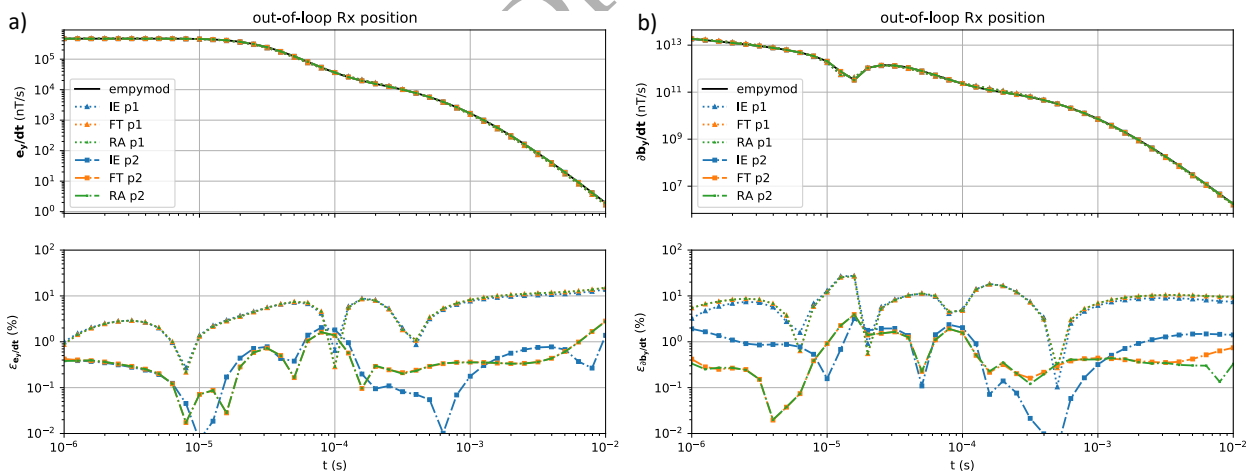

Figure 4. Horizontal y-component of a) magnetic field impulse and b) electric field switch-off step responses at the out-of-loop Rx position (x=150 m, y=100 m), computed with all three approaches and p1 or p2, respectively.

Table 1. Performance of IE, FT and RA approaches in Examples #1 & #2.

Ex.	p	dof (k)	n_{mpi}	n_{omp}	approach	CT (min)	RAM (GB)
#1	1	121	8	1	IE	2.4	3
#1	1	242	12	1	FT	8	4
#1	1	121	8	1	RA	0.2	5
#1	2	660	16	2	IE	14	28
#1	2	1320	22	2	FT	54	45
#1	2	660	16	2	RA	1.3	53
#2	2	674	16	2	IE	19	30
#2	2	1348	22	2	FT	51	41
#2	2	674	16	2	RA	1.8	56
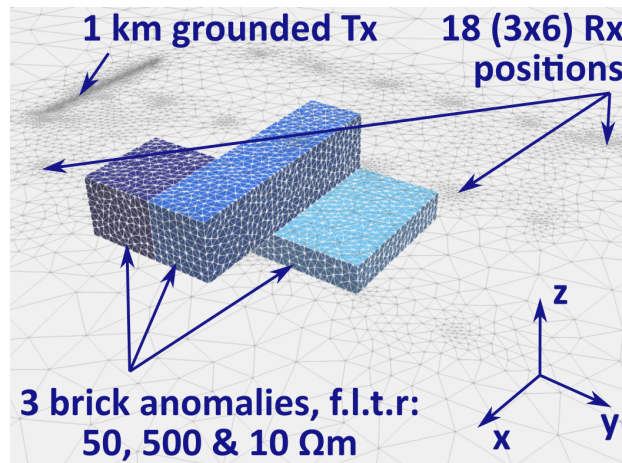
Figure 5. Mesh design for Example #2: halfspace ($100\,\Omega$m) model with three brick anomalies (details in **Table 2**), a 1 km grounded (x-directed) Tx at $y = z = 0$ km and three surface Rx lines at x = (-1, 0, 1) km with each 6 positions at y = (0.5, 1, 1.5, 2, 2.5, 3) km.

Table 2. Description of brick anomalies in **Figure 5**, llc: lower left corner, urc:upper right corner.

anomaly	ρ (Ωm)	(x,y,z) llc (m)	(x,y,z) urc (m)
dark blue	50	(100, 500, -600)	(700, 1000, -200)
blue	500	(-900, 1000, -600)	(700, 1400, -200)
cyan	10	(-900, 1000, -800)	(100, 2000, -600)

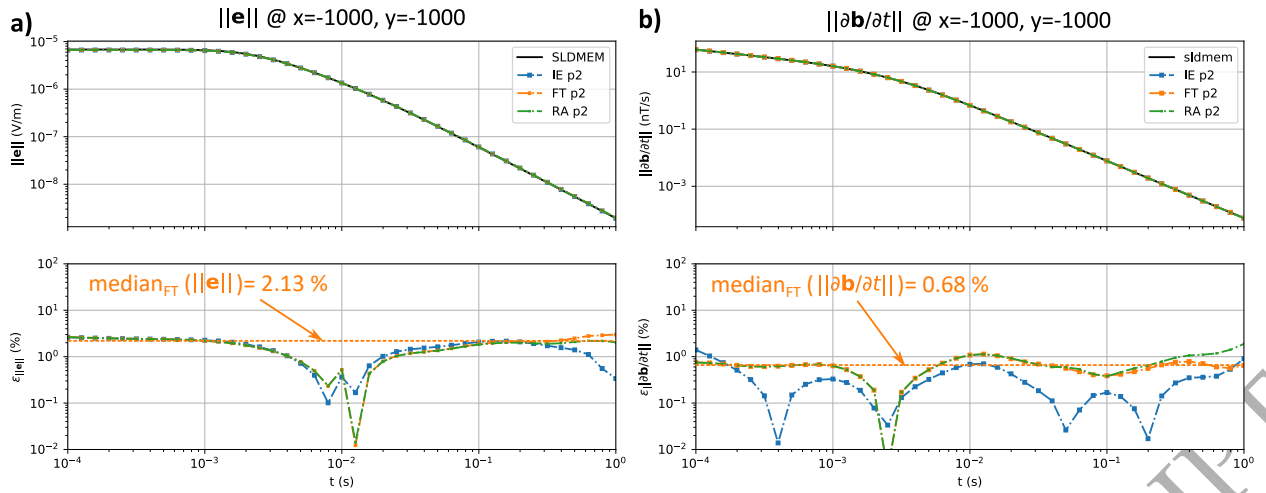**Figure 6.** Magnitude of a) electric field and b) magnetic impulse responses at the position x = 1000 m, y = -1000 m close to the anomalies, dashed orange line is an example for the median levels shown in **Figure 7**.

are listed in **Table 1**. Approximately one hour was required for each of the six *SLDMEM* computations on a single Intel i7-8665U mobile CPU.

Figure 6a) shows the comparison of the e-field vector magnitude, denoted as $||\mathbf{e}||$, at the position x = 1000 m, y = -1000 m close to the anomalies. The related misfits between all *custEM* simulations and the *SLDMEM* solution at this Rx position were smaller than 3 %. **Figure 6**b) presents the corresponding $||\partial \mathbf{b}/\partial t||$ results with NRMS values mainly below 1 %. Tests revealed that the different overall misfit levels are mainly influenced by the underlying *SLDMEM* grid discretization. Viewing further Rx locations (plots are available in the data repository: https://gitlab.com/Rochlitz.R/custEM, 30.11.2020), we observed early-time misfits (<1 ms) of 1 - 10 % and a good agreement of less than 2 %, often better, at later times. Our three results differed at some locations only at late times (>0.1 s), which was mainly caused by effects of handling the DC level in the different approaches.

Figure 7 provides a comprehensive overview of all misfits at the 18 Rx locations. It shows the median (color coded patches) of the 41 NRMS values of each transient response for $||\mathbf{e}||$ (top row) and $||\partial \mathbf{b}/\partial t||$ (bottom row). Bluish colors indicate stations with a very good fit, reddish indicate higher misfits of up to a few percents for most of the data points. The overall agreement of the $||\partial \mathbf{b}/\partial t||$ results with median NRMS values of about 1 % and smaller was very good. The misfit distribution of e varied stronger between the locations and exhibited median values up to 4 %, in particular, on the +1km observation line. We strongly assume that further modifications on the *SLDMEM* grid for e on this Rx line would lead to a better match.

4.3   Example #3: Marlim R3D

After presenting all approached for two land-based setups, our final application is a real-world example about marine CSEM hydrocarbon exploration. Since the **RA** method has shown to be overall as accurate as the other approaches, but significantly faster, we present only results of this method for this example. Recently, Carvalho & Menezes (2017)

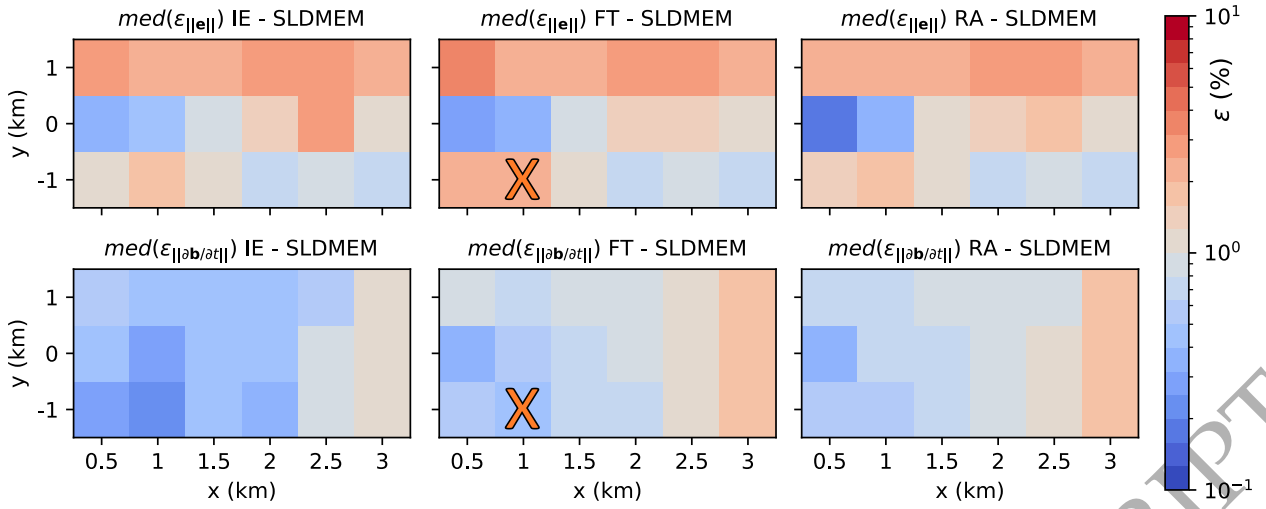**Figure 7.** Color coded median of the 41 NRMS values between 0.1 ms and 1 s at all 18 Rx positions, top row: $||\mathbf{e}||$, bottom row: $||\partial\mathbf{b}/\partial t||$, f.l.t.r: **IE**, **FT**, & **RA** compared to *SLDMEM* solutions, orange "X" mark the values for the transients shown in **Figure 6**.

and Correa & Menezes (2019) (C&M) present the Marlim R3D resistivity model based on an industry dataset from postsalt turbiditic reservoirs at the Brazilian offshore margin. They provide simulated frequency-domain data between 0.1 and 1.25 Hz, obtained with the $\mathcal{TD}$ finite-difference solver *SBLwiz* from EMGS. Following C&M, we utilized reciprocal Tx and Rx positions to decrease the number of sources (solutions of additional right-hand-sides) to be simulated. We compared our $\mathcal{TD}$ solutions of the **RA** method against this recently published $\mathcal{FD}$ reference dataset by transforming the transients into frequency domain. For this task, we applied the *FFTlog* algorithm (Talman 1978; Hamilton 2000) which was reimplemented as *pyfftlog* software in Python by Dieter Werthmüller (`https://github.com/prisae/pyfftlog`, 06.10.2020). The transformation parameters used in this work were added in Appendix D.

The Marlim R3D model includes bathymetry, six subsurface layers with topography obtained from picking horizons in seismic data, and vertical transverse isotropic (VTI) conductivities. The particular challenge for reproducing these results with our code was the mapping of conductivities from a regular grid on a suitable tetrahedral mesh, taking the geometric constraints of the stratigraphic horizons into account. The latter covered only the central part of the area ($\approx$11 km in x- and y-direction from the origin). Beyond this area, we appended an inner and outer boundary mesh for increasing the overall extent to avoid boundary artifacts. Within the inner boundary mesh, the tetrahedra volume was constrained for ensuring an accurate inter- and extrapolation of the supplied resistivity information. **Figure 8** illustrates a section through the complete domain, showing the layered-earth constraints as well as the horizontal resistivity distribution of our mesh. The vertical resistivities are twice as high aside from the air, water and deep salt (on top of basement) layers (Correa & Menezes 2019).

Figure 9 shows the electric fields on the broadside observation line and the corresponding NRMS values compared with the results by Correa & Menezes (2019), Figure 4. The strongest E_x component exhibited mainly misfits
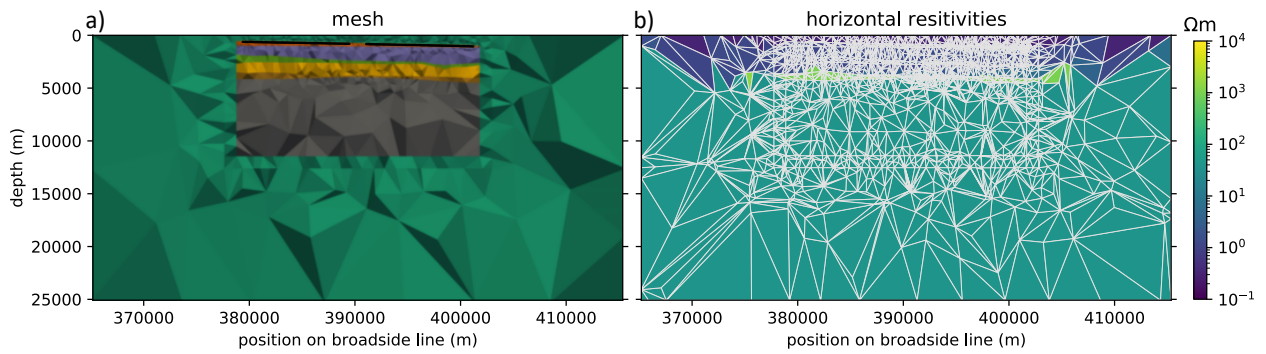
Figure 8. Mesh design of Example #3, the Marlim R3D model, on the vertical (x-z) slice along the broadside observation line, a) "crinkled" view on the six layers (indicated by different colors) in the central part and the surrounding boundary mesh, observation points are indicated as black dots, b) interpolated (central part) and extrapolated (boundary mesh) resistivity distribution on a straight slice (the sliced tetrahedra appear distorted).

below 10 % at all frequencies. The misfits of the weaker E_y & E_z components were overall below 20 %. According to the nature of relative errors, the values were higher at positions of sign reversals or very low signal amplitudes.

In Appendix E, we added a cross-comparison with the *custEM* $\mathcal{FD}$ solution (Werthmüller et al. 2020) for the two frequencies 0.25 Hz and 1 Hz. It revealed that the transformation process from $\mathcal{TD}$ to $\mathcal{FD}$ appeared to be an additional error source in the range of a few percent.

We used the same mesh for the $\mathcal{TD}$ and $\mathcal{FD}$ simulations because the mesh size is mainly controlled by approximating the subsurface geometry. The **RA** approach required ≈5 min computation time with 16 *MPI* processes and 4 *OpenMP* threads. Calculating the results directly in $\mathcal{FD}$ demanded ≈15 min with equal resources. As the transformation effort was negligible, we achieved a performance benefit of factor 3 for this particular example by simulating $\mathcal{FD}$ data in $\mathcal{TD}$ with the **RA** method. This ratio could change with other discretizations and solver types. It could also vary if multiple meshes are designed for specific ranges of times or frequencies in other modeling cases with a less tetrahedra-demanding geometry of the subsurface.
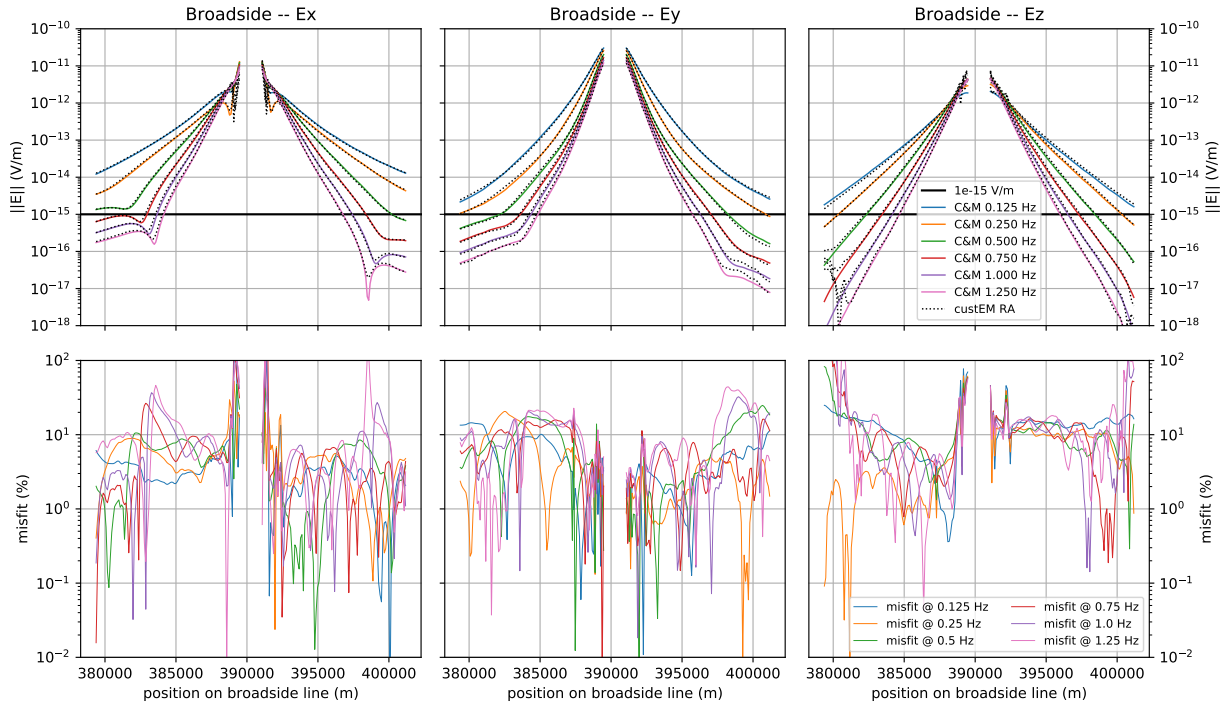
Figure 9. Electric fields and corresponding NRMS values of the **RA** solution compared to the results by Correa & Menezes (2019) (Figure 4) on the broadside observation line, solid line indicates common noise level of 1e-15 V/m.

5 DISCUSSION

5.1 Approach characteristics

All three implemented time-domain EM modeling approaches support the simulation of complex geophysical models with good accuracy, which is mainly determined by the spatial discretization. The **IE** approach was computationally more efficient than the **FT** approach. The **RA** approach clearly outperformed the other two approaches regarding the computation times (**Table 1**). This behavior is related to the computational complexity of each method. Following Mulder et al. (2008) and Börner et al. (2015), we can express the computational efforts as $\mathcal{O}(n_{\text{dof}} * n_{\text{timesteps}})$, $\mathcal{O}(2n_{\text{dof}} * n_{\text{frequencies}})$ (complex-valued systems), and $\mathcal{O}(n_{\text{dof}} * n_{\text{poles}})$ for the **IE**, **FT**, and **RA** approaches, respectively. Taking into account the amount of expensive matrix factorizations using direct solvers, which are primarily controlling the computation times, the representation above is misleading. With our methodology, the computation times depend mainly on the number of logarithmic time steps $+1$, the number of frequencies, and the number of cyclically repeated poles $+1$. **Table 3** provides an overview of these and further characteristics of each approach.

In this work, we only considered simple current wave-forms as ramp effects can often be neglected in case of fast-switching transmitters or irrelevant early times. If realistic ramps are of interest, the current function can be arbitrarily discretized in the **IE** approach and, for instance, adapted in a post-processing step for the **FT** and **RA** approaches Fitterman & Anderson (1987). It is not trivial to calculate sensitivities for inverse modelings with the given formulation

Table 3. Characteristics of the three time-domain modeling approaches related to the implementation in *custEM*.

	comments	IE	FT	RA
matrix factorizations	primarily controlling computation times	number of log. steps +1	number of frequencies	3
comput. time	differs significantly	$\approx 10 \cdot$ **RA**	$\approx 3\text{-}4 \cdot$ **IE**	very fast
mainly dependent on:	all approaches: spatial discretization, polynomial order & domain extent	lin/log time steps	number of frequencies	number of poles
memory consumption	overall huge because of the direct solver	huge	$\approx 2 \cdot$ **IE**	$\approx 2 \cdot$ **IE**
accuracy	with second order polynomials	high	high	high
mainly dependent on:	all approaches: spatial discretization, polynomial order & domain extent	time discretization	FHT parameters, freq	choice of poles
transmitter waveforms	support of non-ideal switch-on and switch-off processes	yes	adaption of FHT or post-processing	only with post-processing
coverage in time	decades covered with one mesh and sufficient accuracy (in general)	five to six	six or more	four to five
anisotropy	support of general anisotropic material properties	yes	yes	yes
induced polarization	support of Cole-Cole models	not yet	yes	not yet

of the **RA** approach. To the best of our knowledge, it has not yet been possible to develop an algorithm for calculating the derivatives of the Krylov basis vectors (25) with respect to the electrical conductivity.

Projecting the results at points in time is computationally inexpensive in the **RA** approach. Therefore, the numerical integration method for obtaining b from $\dot{\text{b}}$ is efficient. In contrast, numerical integration is unsuited for the other two approaches. It requires a denser logarithmic spacing in time or significantly more frequency solutions to be calculated, which would make the computational performance even worse.

Based on the overall performance, it appears that the **RA** approach is the method of choice. In combination with the logarithmic Fast Fourier transformation *logfft*, the **RA** approach can be seriously considered as an alternative to simulations in the frequency-domain. Even though not considered here, the poles ξ introduced in the **RA** method can be used to directly compute the frequency-domain response for a given spatial discretization.

5.2   Validation

To the best of our knowledge, there is still no report about proposals for a standard to evaluate the accuracy of 3D geophysical EM simulations. With respect to recently published research, we consider misfits of less than 1 % between 3D numerical and semi-analytic solutions as sufficiently accurate. Accordingly, we achieved good results with p2 basis functions in Example #1, whereas the p1 results were not accurate enough with errors up to 10 %. We decided for p1 and p2 computations on the same mesh in this examples for directly comparing accuracy and performance.

We observed increased errors of the p2 results towards the latest observation times in Example #1. The late-time errors were caused by the horizontal limitation of the layered-earth extent of the mesh as a compromise between accuracy and computational performance. Shifting the boundary-mesh to a greater distance would reduce the boundary effects for the cost of longer computation times and higher memory requirements. These boundary effects were not visible in the p1 results due to the greater overall error level caused by the comparatively coarse refinement.

Simulations with p1 can of course provide better results by using finer meshes with higher quality (Rochlitz 2020). However, this would lead to an inferior computational performance compared to the p2 computations (Grayver & Kolev 2015; Rochlitz et al. 2019; Castillo-Reyes et al. 2019). Nevertheless, we regard p1 simulations as a very practical tool for getting a first impression of the EM field behavior of realistic models and for simulating complicated geometries which already have a large number of tetrahedra after the mesh generation, even without considering further Rx or Tx refinements.

We also expected misfits of around 1 % for accurate results of two different numerical codes, simulating exactly the same geometry in Example #2. Our comparison showed error levels of a few percent and less for the majority of the compared data points, but also larger misfits of up to more than 10 % at a few Rx locations. The median value was chosen instead of the mean as overall estimate of the fit between two different results to avoid the influence of single data points with very high relative errors due to very low amplitudes or sign reversals. The even better choice for an overall error estimate can be other percentiles, e.g., the 90th percentile instead of the median as 50th percentile Rochlitz (2020). This would guaranty that almost all (e.g., 90%) data points are of better quality than this measure. Moreover, the specific percentile can be chosen according to the number of investigated data points and expected outliers.

Aside from varying the spatial discretization and simulation parameters to optimize the fit between our two independent simulations, a validation of the "true" result would be only possible through a cross-validation with further codes. In contrast to Example #1, a homogeneous subsurface model with multiple single anomalies of arbitrary shape is suited for an unstructured tetrahedral discretization. Table 1 shows comparable computational efforts for the simple 1D TEM and the 3D LOTEM model as a strong argument for this statement.

In Example #3, the published FD model results were independently reproduced based on the information by Correa & Menezes (2019). Actually, the unstructured tetrahedral discretization is generally suited to approximate realistic, irregular geometries such as in Marlim R3D with subsurface layer constraints. However, the provided resistivity model on a fine, regular grid with a limited extent required the interpolation of the resistivity distribution on our tetrahedral

elements. We assume this procedure to cause the higher misfits up to 20 % and are aware of the related discrepancies. Though, this example demonstrates very well the unavoidable issue of a common and realistic model representation between different numerical methods in practical modeling applications.

Due to this problem and as further mesh variations did not yield better matching results, we considered the average error of 10 % as sufficient for the Marlim R3D model cross-comparison. This reveals that there is still a requirement of comparing more real-world models between state-of-the-art EM codes instead of validations to semi-analytic solutions for confirming the general accuracy. We think the most challenging part in complex geophysical EM modeling is to represent the true geometry of complicated conductivity structures accurately while keeping the required computational resources low.

5.3 Enhancements

The implementation of alternative iterative solvers with appropriate preconditioners would reduce the memory requirements significantly. Even though a broad range of preconditioners and iterative solution methods are provided by *FEniCS* and *PETSc*, this development step would require huge efforts for analyzing the approach-specific, poorly conditioned system-matrices arising from the FE formulation to solve EM problems on unstructured tetrahedral meshes with tremendously varying cell sizes.

Adaptive time-stepping techniques as an alternative to our fixed logarithmic spacing with internal linear steps could provide a higher flexibility to enhance the computational performance of the **IE** approach. The performance of the **FT** approach can be considerably improved with a smaller number of problem-dependent FHT filter coefficients for specific setups Werthmüller et al. (2021). For instance, reducing the amount of required frequencies from 120 to 20-30 would speed up the **FT** approach significantly and make it maybe even faster than the **IE** method. Moreover, we assume that it would be worth investigating if the sequence of frequency-domain simulations in the **FT** method could be calculated faster with optimized iterative solution strategies for such problems.

6 CONCLUSIONS

We present a direct comparison of three of the most common approaches for modeling 3D transient electromagnetic data. Three examples ranging from simple to challenging EM modeling environments illustrate the numerical accuracy, computational performance, and unique characteristics of all implemented approaches. The implicit Euler and inverse Fourier Transform based approaches are computationally not competitive to the Rational Arnoldi method in our work using unstructured tetrahedral meshes and the direct solver MUMPS. It is worth mentioning that simulations based on other numerical methods, discretizations and iterative solvers could lead to contrary observations.

We are confident that it would be possible to improve the computational performance of the **IE** and **FT** approaches using our discussed options and maybe others, whereas we do not see any straightforward and significant optimization potential for the **RA** method as used in our work. In particular, where is a great potential to reduce the number of required frequencies for the **FT** approach which would make it absolutely competitive to the **IE** approach in terms of computation times.

Nevertheless, the **RA** method, which requires only three expensive matrix factorizations with our implementation, would still clearly outperform the other approaches. We expect the parallelized version of the computationally most efficient Rational Arnoldi method to be of great use for the simulation of 3D TEM signals. Our final example shows that in some cases, calculating frequency-domain responses with the time-domain Rational Arnoldi method might be beneficial over computations in frequency domain. We are convinced that the topic of converting time-domain responses into frequency-domain is worth further investigation.

We provide an open-source, parallelized FE implementation for efficiently simulating realistic 3D time-domain EM data. We encourage geophysical EM modelers to prefer benchmarking their codes with realistic 3D models via cross-comparisons over validations to semi-analytic solutions since nowadays, the challenge in 3D geophysical EM modeling appears to be not anymore the implementation of the numerical methods but the optimum discretization of realistic 3D survey geometries. In this context, we are open for participating in further benchmark studies or for comparing the results of this work with others.

7 ACKNOWLEDGMENTS

8 DATA AVAILABILITY

The open-source toolbox *custEM* and all presented results can be accessed on https://gitlab.com/Rochlitz.R/custEM, (30.11.2020). The documentation is available on https://custem.readthedocs.io, (30.11.2020). The software and corresponding data can be used for individual purposes by following the GNU General Public License, version 3.

REFERENCES

Alumbaugh, D. L., Newman, G. A., Prevost, L., & Shadid, J. N., 1996. Three-dimensional wideband electromagnetic modeling on massively parallel computers, *Radio Science*, **31**(1), 1–23.

Andersen, W. L., 1989. A hybrid fast hankel transform algorithm for electromagnetic modeling, *Geophysics*, **54**(2), 263–266.

Anderson, W. L., 1973. *Fortran IV Programs: For the Determination of the Transient Tangential Electrical Field and Vertical Magnetic Field about a Vertical Magnetic Dipole for an M-layer Stratified Earth by Numerical Integration and Digital Linear Filtering*, US Geological Survey.

Badea, E. A., Everett, M. E., Newman, G. A., & Biro, O., 2001. Finite-element analysis of controlled-source electromagnetic induction using coulomb-gauged potentials, *Geophysics*, **66**(3), 786–799.

Bello, M. A., Guo, R., & Liu, J., 2019. Forward plane-wave electromagnetic model in three dimensions using hybrid finite volume–integral equation scheme, *Geophysical Prospecting*, **67**(8), 2213–2226.

Börner, R.-U., 2010. Numerical modelling in geo-electromagnetics: advances and challenges, *Surveys in Geophysics*, **31**(2), 225–245.

Börner, R.-U., Ernst, O. G., & Spitzer, K., 2008. Fast 3-D simulation of transient electromagnetic fields by model reduction in the frequency domain using krylov subspace projection, *Geophysical Journal International*, **173**(3), 766–780.

Börner, R.-U., Ernst, O. G., & Güttel, S., 2015. Three-dimensional transient electromagnetic modelling using rational Krylov methods, *Geophysical Journal International*, **202**(3), 2025–2043.

Cai, H., Hu, X., Xiong, B., Auken, E., Han, M., & Li, J., 2017. Finite element time domain modeling of controlled-source electromagnetic data with a hybrid boundary condition, *Journal of Applied Geophysics*, **145**, 133–143.

Carvalho, B. R. & Menezes, P. T. L., 2017. Marlim R3D: a realistic model for CSEM simulations-phase I: model building, *Brazilian Journal of Geology*, **47**(4), 633–644.

Castillo-Reyes, O., de la Puente, J., & Cela, J. M., 2018. PETGEM: A parallel code for 3D CSEM forward modeling using edge finite elements, *Computers & Geosciences*, **119**, 123–136.

Castillo-Reyes, O., de la Puente, J., García-Castillo, L. E., & Cela, J. M., 2019. Parallel 3-D marine controlled-source electromagnetic modelling using high-order tetrahedral nédélec elements, *Geophysical Journal International*, **219**(1), 39–65.

Cherevatova, M., Egbert, G., & Smirnov, M. Y., 2018. A multi-resolution approach to electromagnetic modelling, *Geophysical Journal International*, **214**(1), 656–671.

Christensen, N. B., 1990. Optimized fast hankel transform filters, *Geophysical Prospecting*, **38**, 545–568.

Cockett, R., Kang, S., Heagy, L. J., Pidlisecky, A., & Oldenburg, D. W., 2015. SimPEG: An open source framework for simulation and gradient based parameter estimation in geophysical applications, *Computers & Geosciences*, **85**, 142–154.

Coggon, J., 1971. Electromagnetic and electrical modeling by the finite element method, *Geophysics*, **36**(1), 132–155.

Commer, M. & Newman, G., 2004. A parallel finite-difference approach for 3D transient electromagnetic modeling with galvanic sources, *Geophysics*, **69**(5), 1192–1202.

Constable, S., 2010. Ten years of marine CSEM for hydrocarbon exploration, *Geophysics*, **75**(5), 75A67–75A81.

Correa, J. L. & Menezes, P. T., 2019. Marlim R3D: A realistic model for controlled-source electromagnetic simulations-phase 2: The controlled-source electromagnetic data set, *Geophysics*, **84**(5), E293–E299.

Druskin, V. & Knizhnerman, L., 1994. Spectral approach to solving three-dimensional Maxwell's diffusion equations in the time and frequency domains, *Radio Science*, **29**(4), 937–953.

Druskin, V. L. & Knizhnerman, L., 1988. Spectral differential-difference method for numeric solution of three-dimensional nonstationary problems of electric prospecting, *Earth Physics*, **24**(8), 641–648.

Farquharson, C. G. & Miensopust, M. P., 2011. Three-dimensional finite-element modelling of magnetotelluric data with a divergence correction, *Journal of Applied Geophysics*, **75**(4), 699–710.

Fitterman, D. V. & Anderson, W. L., 1987. Effect of transmitter turn-off time on transient soundings, *Geoexploration*, **24**(2), 131–146.

Ghosh, D. P., 1971. The application of linear filter theory to the direct interpretation of geoelectrical resistivity sounding measurements, *Geophysical Prospecting*, **19**, 192–217.

Goldman, M. & Stoyer, C., 1983. Finite-difference calculations of the transient field of an axially symmetric earth for vertical magnetic dipole excitation, *Geophysics*, **48**(7), 953–963.

Grayver, A. V. & Kolev, T. V., 2015. Large-scale 3D geoelectromagnetic modeling using parallel adaptive high-order finite element method, *Geophysics*, **80**(6), E277–E291.

Guo, Z., Xue, G., Liu, J., & Wu, X., 2020. Electromagnetic methods for mineral exploration in China: A review, *Ore Geology Reviews*, **118**, 103357.

Haber, E., Ascher, U., Aruliah, D., & Oldenburg, D., 2000. Fast simulation of 3D electromagnetic problems using potentials, *Journal of Computational Physics*, **163**(1), 150–171.

Hamilton, A., 2000. Uncorrelated modes of the non-linear power spectrum, *Monthly Notices of the Royal Astronomical Society*, **312**(2), 257–284.

Heagy, L. J., Kang, S., Cockett, R., & Oldenburg, D. W., 2020. Open-source software for simulations and inversions of airborne electromagnetic data, *Exploration Geophysics*, **51**(1), 38–44.

Hohmann, G. W., 1975. Three-dimensional induced polarization and electromagnetic modeling, *Geophysics*, **40**(2), 309–324.

Huang, X., Yin, C., Farquharson, C. G., Cao, X., Zhang, B., Huang, W., & Cai, J., 2019. Spectral-element method with arbitrary hexahedron meshes for time-domain 3D airborne electromagnetic forward modeling, *Geophysics*, **84**(1), E37–E46.

Jin, J.-M., 2015. *The finite element method in electromagnetics*, John Wiley & Sons.

Johansen, H. K. & Sørensen, K., 1979. Fast Hankel transforms, *Geophysical Prospecting*, **27**, 876–901.

Kamm, J., Becken, M., & Abreu, R., 2020. Electromagnetic modelling with topography on regular grids with equivalent materials, *Geophysical Journal International*, **220**(3), 2021–2038.

Kaufman, A. A., Keller, G. V., et al., 1983. Frequency and transient soundings, *Chi-Yu King Roberto Scarpa*, **207**.

Key, K., 2012a. Is the fast Hankel transform faster than quadrature?, *Geophysics*, **77**(3), F21–F30.

Key, K., 2012b. Marine electromagnetic studies of seafloor resources and tectonics, *Surveys in geophysics*, **33**(1), 135–167.

Kruglyakov, M. & Kuvshinov, A., 2019. 3-D inversion of MT impedances and inter-site tensors, individually and jointly. New lessons learnt, *Earth, Planets and Space*, **71**(1), 4.

Langtangen, H. P., Logg, A., & Tveito, A., 2016. *Solving PDEs in Python: The FEniCS Tutorial I*, Springer International Publishing.

Lin, C., Zhong, S., Auken, E., Cai, H., Tan, H., Peng, M., & Kong, W., 2018. The effects of 3D topography on controlled-source audio-frequency magnetotelluric responses, *Geophysics*, **83**(2), WB97–WB108.

Liu, Y., Xu, Z., & Li, Y., 2018a. Adaptive finite element modelling of three-dimensional magnetotelluric fields in general anisotropic media, *Journal of Applied Geophysics*, **151**, 113–124.

Logg, A., Mardal, K.-A., & Wells, G., 2012. *Automated solution of differential equations by the finite element method: The FEniCS book*, vol. 84, Springer Science & Business Media.

Long, J. & Farquharson, C. G., 2019. On the forward modelling of three-dimensional magnetotelluric data using a radial-basis-function-based mesh-free method, *Geophysical Journal International*, **219**(1), 394–416.

Lu, J., Li, Y., & Du, Z., 2019. Fictitious wave domain modelling and analysis of marine CSEM data, *Geophysical Journal International*, **219**(1), 223–238.

Madsen, N. K. & Ziolkowski, R. W., 1990. A three-dimensional modified finite volume technique for maxwell's equations, *Electromagnetics*, **10**(1-2), 147–161.

Miensopust, M. P., 2017. Application of 3-D electromagnetic inversion in practice: Challenges, pitfalls and solution approaches, *Surveys in Geophysics*, **38**(5), 869–933.

Mohsen, A. A. & Hashish, E. A., 1994. The fast Hankel transform, *Geophysical Prospecting*, **42**, 131–139.

Mulder, W. A., Wirianto, M., & Slob, E. C., 2008. Time-domain modeling of electromagnetic diffusion with a frequency-domain code, *Geophysics*, **73**(1), F1–F8.

Nédélec, J.-C., 1980. Mixed finite elements in $\mathbf{R}^3$, *Numerische Mathematik*, **35**(3), 315–341.

Oristaglio, M., 1982. Diffusion of electromagnetic fields into the earth from a line source of current, *Geophysics*, **47**(11), 1585–1592.

Pridmore, D., Hohmann, G., Ward, S., & Sill, W., 1981. An investigation of finite-element modeling for

electrical and electromagnetic data in three dimensions, *Geophysics*, **46**(7), 1009–1024.

Qi, Y., El-Kaliouby, H., Revil, A., Ahmed, A. S., Ghorbani, A., & Li, J., 2019. Three-dimensional modeling of frequency-and time-domain electromagnetic methods with induced polarization effects, *Computers & geosciences*, **124**, 85–92.

Qiu, C., Güttel, S., Ren, X., Yin, C., Liu, Y., Zhang, B., & Egbert, G., 2019b. A block rational Krylov method for 3-D time-domain marine controlled-source electromagnetic modelling, *Geophysical Journal International*, **218**(1), 100–113.

Raiche, A., 1974. An integral equation approach to three-dimensional modelling, *Geophysical Journal International*, **36**(2), 363–376.

Raiche, A., Sugeng, F., & Wilson, G., 2007. Practical 3D EM inversion? The P223F software suite, *ASEG Extended Abstracts*, **2007**(1), 1–5.

Ren, Z., Kalscheuer, T., Greenhalgh, S., & Maurer, H., 2013. A goal-oriented adaptive finite-element approach for plane wave 3-D electromagnetic modelling, *Geophysical Journal International*, **194**(2), 700–718.

Rochlitz, R., 2020. *Analysis and open-source Implementation of Finite Element Modeling techniques for Controlled-Source Electromagnetics*, Ph.D. thesis, Westfälische Wilhelms-Universität Münster.

Rochlitz, R., Queitsch, M., Yogeshwar, P., Günther, T., Chwala, A., Janser, S., Kukowski, N., & Stolz, R., 2018. Capability of low-temperature SQUID for transient electromagnetics under anthropogenic noise conditions, *Geophysics*, **83**(6), E371–E383.

Rochlitz, R., Skibbe, N., & Günther, T., 2019. custEM: Customizable finite-element simulation of complex controlled-source electromagnetic data, *Geophysics*, **84**(2), F17–F33.

Rücker, C., Günther, T., & Wagner, F., 2017. pyGIMLi: An open-source library for modelling and inversion in geophysics, *Computers & Geosciences*, **109**, 106–123.

Schmucker, U. & Weidelt, P., 1975. Electromagnetic induction in the earth, *Lecture Notes, Aarhus Univ., Denmark*.

Schwarzbach, C., Börner, R.-U., & Spitzer, K., 2011. Three-dimensional adaptive higher order finite element simulation for geo-electromagnetics – a marine CSEM example, *Geophysical Journal International*, **187**(1), 63–74.

Seidel, M., 2019. *A 3D Time Domain CSEM Forward Modeling Code using custEM and FEniCS*, Ph.D. thesis, University of Cologne.

Si, H., 2015. TetGen, a Delaunay-based quality tetrahedral mesh generator, *ACM Transactions on Mathematical Software (TOMS)*, **41**(2), 11.

Siemon, B., Christiansen, A. V., & Auken, E., 2009. A review of helicopter-borne electromagnetic methods for groundwater exploration, *Near Surface Geophysics*, **7**(5-6), 629–646.

Skibbe, N., Rochlitz, R., Günther, T., & Müller-Petke, M., 2020. Comet: An open-source toolbox for

surface NMR, *Geophysics*, **85**(3), 1–56.

Smith, R., 2014. Electromagnetic induction methods in mining geophysics from 2008 to 2012, *Surveys in Geophysics*, **35**(1), 123–156.

Talman, J. D., 1978. Numerical fourier and bessel transforms in logarithmic variables, *Journal of computational physics*, **29**(1), 35–48.

Um, E. S., Harris, J. M., & Alumbaugh, D. L., 2010. 3D time-domain simulation of electromagnetic diffusion phenomena: A finite-element electric-field approach, *Geophysics*, **75**(4), F115–F126.

Um, E. S., Harris, J. M., & Alumbaugh, D. L., 2012. An iterative finite element time-domain method for simulating three-dimensional electromagnetic diffusion in earth, *Geophysical Journal International*, **190**(2), 871–886.

Wang, T. & Hohmann, G. W., 1993. A finite-difference, time-domain solution for three-dimensional electromagnetic modeling, *Geophysics*, **58**(6), 797–809.

Ward, S. H. & Hohmann, G. W., 1988. Electromagnetic theory for geophysical applications, in *Electromagnetic methods in applied geophysics*, vol. 1, pp. 131–311.

Werthmüller, D., 2017. An open-source full 3D electromagnetic modeler for 1D VTI media in python: empymod, *Geophysics*, **82**(6), WB9–WB19.

Werthmüller, D., Key, K., & Slob, E. C., 2019a. A tool for designing digital filters for the Hankel and Fourier transforms in potential, diffusive, and wavefield modeling, *Geophysics*, **84**(2), F47–F56.

Werthmüller, D., Mulder, W., & Slob, E., 2019b. emg3d: A multigrid solver for 3D electromagnetic diffusion, *Journal of Open Source Software*, **4**(39), 1463.

Werthmüller, D., Rochlitz, R., Castillo-Reyes, O., & Heagy, L., 2020. Open-source landscape for 3D CSEM modelling, *arXiv preprint arXiv:2010.12926*.

Werthmüller, D., Mulder, W. A., & Slob, E. C., 2021. Fast Fourier transform of electromagnetic data for computationally expensive kernels, *Geophysical Journal International*, **226**(2), 1336–1347.

Yogeshwar, P. & Tezkan, B., 2017. Two-dimensional basement modeling of central loop transient electromagnetic data from the central azraq basin area, jordan, *Journal of Applied Geophysics*, **136**, 198–210.

Appendix A - FHT filter coefficients

Additional to the set of filter weights, a digital filter consists of two more parameters: the shift a and the sampling interval or spacing s. The shift factor a determines the starting point for sampling the input function in the frequency domain and the unit-free spacing s defines the interval for the subsequent samples in the frequency domain down to the lowest frequency. Thus, the set of n sampling frequencies f_n, ordered from high to low, is given by:

$$f_n = \frac{1}{t_0}\frac{a}{s^i}, \quad i = n, ..., 1 , \tag{.1}$$

with t_0, the first time channel. We used the following FHT filter coefficients with the sampling interval s $= 10^{0.1}$ and the shift factor a $= 1.653801536E{+}03$:

5.001828E-11,	8.000316E-11,	1.256402E-10,	2.009589E-10,
3.155941E-10,	5.047858E-10,	7.927364E-10,	1.267965E-09,
1.991264E-09,	3.184983E-09,	5.001829E-09,	8.000316E-09,
1.256403E-08,	2.009589E-08,	3.155941E-08,	5.047858E-08,
7.927363E-08,	1.267965E-07,	1.991263E-07,	3.184982E-07,
5.001826E-07,	8.000310E-07,	1.256401E-06,	2.009585E-06,
3.155931E-06,	5.047835E-06,	7.927307E-06,	1.267950E-05,
1.991228E-05,	3.184892E-05,	5.001599E-05,	7.999741E-05,
1.256258E-04,	2.009226E-04,	3.155029E-04,	5.045568E-04,
7.921612E-04,	1.266520E-03,	1.987636E-03,	3.175872E-03,
4.978954E-03,	7.942905E-03,	1.242000E-02,	1.973483E-02,
3.065536E-02,	4.821916E-02,	7.364350E-02,	1.128325E-01,
1.647498E-01,	2.348622E-01,	3.004906E-01,	3.372419E-01,
2.337323E-01,	-8.647107E-02,	-6.612999E-01,	-8.142974E-01,
3.308580E-01,	1.402432E-00,	-1.565116E-00,	8.359842E-01,
-3.059907E-01,	9.125030E-02,	-2.463153E-02,	6.369876E-03,
-1.618934E-03,	4.085877E-04,	-1.028279E-04,	2.584884E-05,
-6.494904E-06,	1.631643E-06,	-4.098700E-07,	1.029566E-07,
-2.586174E-08,	6.496194E-09,	-1.631772E-09,	4.098828E-10,
-1.029579E-10,	2.586184E-11,	-6.496186E-12,	1.631761E-12

Appendix B - custEM

Reusing established software, *custEM* relies on the open-source library *FEniCS* (Logg et al. 2012; Langtangen et al. 2016), providing highly-developed libraries for the automated solution of partial differential equations. It further uses *TetGen* (Si 2015) and *pyGIMLi* (Rücker et al. 2017) for the mesh generation and *COMET* (Skibbe et al. 2020) for primary field calculations. The modularized organization allowed reusing existing sub-modules for the $\mathcal{TD}$ modeling approaches and also a total-field formulation for calculating 3D natural-source (MT) EM data.

In addition to the major extension by adding the three time-domain modeling approaches as well as an MT modeling approach, we mention further important developments after the previously published version 0.93 (Rochlitz et al. 2019). The provided *conda* package simplifies the installation process for users and reduces incompatibility issues on different computer architectures. Newer *conda* packages of *FEniCS* support parallel I/O of model data and use recent versions of *MUMPS*. This leads to a significant computational performance improvement and the system matrix size is no longer limited. Incorporating multiple sources on multiple right-hand sides of the systems of equations was automated in all approaches, allowing to exploit re-using matrix factorization. In this context, we could remove redundant I/O overhead and add alternative parallelized interpolation methods.

The electric-field modeling approaches in $\mathcal{FD}$ support now simulations with relative magnetic permeabilities and induced polarization parameters. Common total and secondary field potential approaches for solving the DC problem were added. The mesh generation tools contain new features for automatically incorporating bathymetry information to model coastal or marine environments. Further meshing improvements are the support of connected embedded anomalies, an optimized Tx and Rx discretization, automated forwarding of Tx and Rx information for the FE simulation, and general updates to minimize the amount of required tetrahedra for most CSEM geometries.

The open-source Python toolbox *custEM* 1.0 has now become a tool for simulating any kind of CSEM, TEM and MT data, including marine, coastal, land-based, semi-airborne, airborne and borehole models with arbitrary geometry. A variety of supplied tutorials and examples can support interested users in simulating their own EM setups. In addition to forward modeling purposes, it is possible to build inverse-modeling routines upon our implemented algorithms.
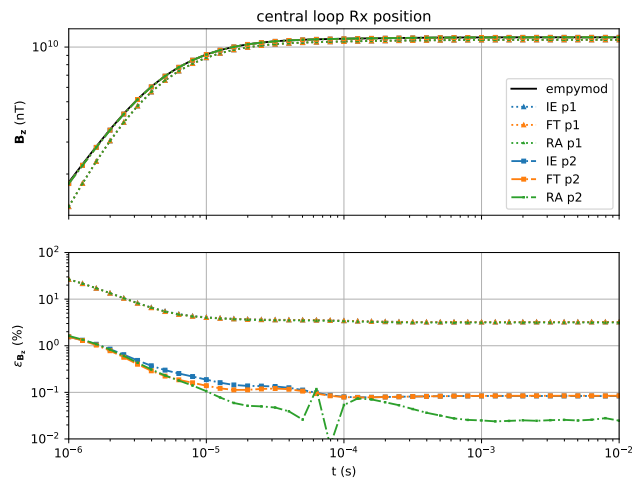
Figure A1. Central loop switch-on b_z transients of p1 and p2 computations of all three approaches.

Appendix C - Magnetic field responses

Figure A1 illustrates the b_z switch-on transients of Example #1 at the central loop positions. Aside from the early times, the relative error levels for p1 and p2 are lower than the ones of the impulse response and switch-off transients in **Figure 3**. This observation can be attributed to the high amplitude level of the static field, which dominates the transients more and more towards late times. There are no boundary effects visible in comparison to the late-time switch-off transients of b, whose quality depends on an accurate estimation of $b_{\texttt{static}}$.
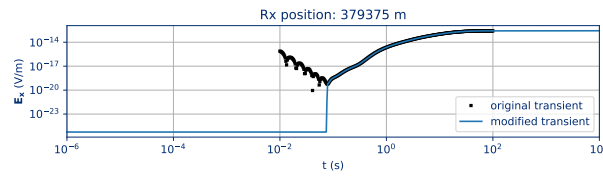
Figure A2. Original RA result and modified transient as input for the *pyfftlog* transformation.

Appendix D - Transformation of transients

The results of testing different parameters showed that the most accurate transformation results with the *fftl* subroutine of the *pyfftlog* algorithm (https://github.com/prisae/pyfftlog, 06.10.2020) were achieved by using a long input time range from 1e-6 to 1e4 s with a fine sampling of 80 logarithmic steps per decade. Furthermore, we set the bias coefficient q = 1. We were required to modify the original RA solution with 80 samples per decade between 1e-2 to 1e2 s for this procedure. First, we determined the signal onset based on a constantly increasing signal and the amplitude level. Second, we set all values before the signal onset to the constant value of the onset amplitude divided by 1e6. Third, we used the *UnivariateSpline* algorithm of the *scipy* library to extent the original signal in both direction in time. **Figure A2** illustrates the modification result for one example transient.
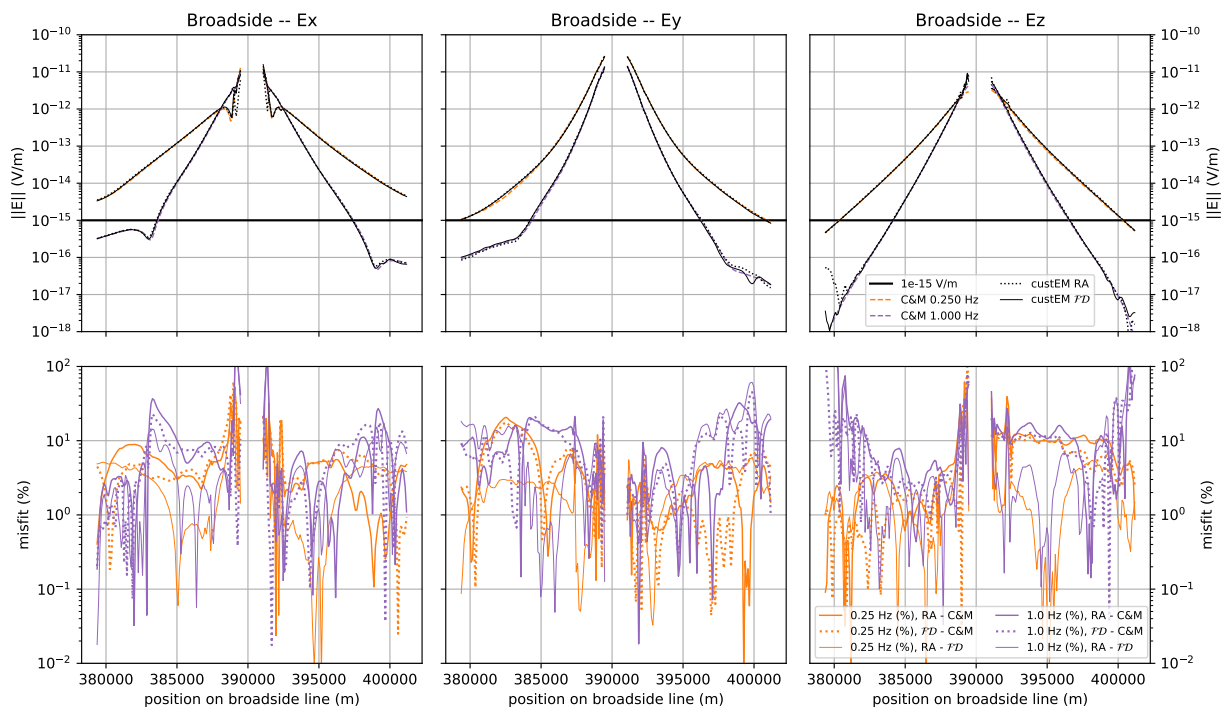
Figure A3. Electric fields and corresponding NRMS values for two frequencies on the broadside observation line, comparison between Correa & Menezes (2019) (C&M), **RA**, and custEM $\mathcal{FD}$ solutions, solid line indicates common noise level of 1e-15 V/m.

Appendix E - Marlim R3D cross-comparison

Figure A3 reveals in many areas higher misfits between both of our and the C&M solutions than between the transformed **RA** and $\mathcal{FD}$ solutions. This indicated a strong influence of the model discretization and resistivity interpolation procedure on the results. In most areas along the profile, the **RA** - C&M misfits were slightly higher than the $\mathcal{FD}$-C&M misfits, which indicated an overall small error contribution by the transformation process. Between 395000 and 400000 m, the fit of the E_x component was better between **RA** - C&M compared to $\mathcal{FD}$-C&M, in particular at 0.25 Hz. This observation demonstrated that also the chosen numerical simulation approach can lead to higher misfits in some areas.